CrossMark
click for updates

Synergistic interactions of Cu and N on surface altered amorphous TiO$_2$ nanoparticles for enhanced photocatalytic oxidative desulfurization of dibenzothiophene†

C. N. C. Hitam,[a] A. A. Jalil,*[ab] S. Triwahyono,[c] A. Ahmad,[ab] N. F. Jaafar,[c] N. Salamun,[c] N. A. A. Fatah,[a] L. P. Teh,[c] N. F. Khusnun[a] and Z. Ghazali[d]

Amorphous TiO$_2$ (AT) nanoparticles were prepared by a simple sol–gel method and subsequent incorporation with copper (5–20 wt%) *via* an electrochemical method in the presence of a supporting electrolyte, tetraethylammonium perchlorate (TEAP), was used to synthesize CuO/TiO$_2$ (CAT) catalysts. The physicochemical properties of the catalysts were studied by XRD, N$_2$ adsorption–desorption, TEM, FTIR, XPS, ESR and UV-Vis DRS. Photocatalytic testing on the oxidative desulfurization of dibenzothiophene (DBT) under UV and visible light irradiation demonstrated that the CAT catalysts were active under both conditions. It was found that Ti^{3+} surface defects (TSD), oxygen vacancies (V$_o$), CuO, Ti–O–N/O–Ti–N and Ti–O–Cu bonds played an important role in photooxidation. The TSD, V$_o$, CuO, N 1s and Cu 2p states in the CAT catalysts acted as electron trappers to hinder electron–hole recombination. In addition, these TSD, V$_o$, N 1s and Cu 2p species also contributed to the lowering of the CAT band gap, which enabled photooxidation to be carried out in the visible light region. The photooxidation followed a pseudo-first order Langmuir–Hinshelwood model with adsorption being the controlling step.

1. Introduction

Sulfur oxides (SO$_x$) resulting from the combustion of sulfur compounds in fuels have become one of the most serious environmental problems, as they are a major source of acid rain, global warming and atmospheric pollution.[1] In addition, sulfur emissions also cause respiratory sicknesses, aggravate heart disease and trigger asthma.[2] In order to minimize the negative health and environmental effects, more rigid regulations are entrenched to reduce the sulfur concentration limits in gasoline. A conventional desulfurization technology is hydrodesulfurization (HDS), which is highly efficient in removing aliphatic and acyclic sulfur-containing compounds, such as thiols, sulfides, disulfides and other sulfur compounds, by transforming them to hydrogen sulfide.[3] However, the HDS technology is not suitable for further reduction of sulfur content because it requires high temperatures, pressures and operational costs. Hence, other approaches have been applied for desulfurization in order to overcome such shortcomings, these include biodesulfurization (BDS), adsorptive desulfurization (ADS) and extractive desulfurization (EDS). Among all these methods, oxidative desulfurization (ODS) is one of the most capable ways to complement HDS due to its mild operating conditions, low cost, no hydrogen consumption and high efficiency.[4] However, the operating temperature led to side reactions that reduce the overall octane rating of the fuel.[5] Recently, photocatalytic oxidative desulfurization (PODS) has become more popular because it can be conducted under mild conditions and converts toxic organic pollutants into non-toxic products with high product selectivity.[6,7]

Among the various types of photocatalysts, TiO$_2$ has been widely used for degradation of organic pollutants due to its low cost, non-toxicity, high chemical stability and photocatalytic activity.[8] However, some limitations, such as its high recombination rate of photogenerated electron–hole pairs and its wide band gap, hinder its photocatalytic efficiency.[9,10] Therefore, various strategies have been developed to alter the properties of TiO$_2$, including doping with transition metal elements which are able to increase its charge separation efficiency and visible-light sensitivity.[11] Meanwhile, most of the efforts so far have

[a]*Department of Chemical Engineering, Faculty of Chemical Engineering, Universiti Teknologi Malaysia, 81310 UTM Johor Bahru, Johor, Malaysia. E-mail: aishahaj@utm.my*

[b]*Centre of Hydrogen Energy, Institute of Future Energy, Universiti Teknologi Malaysia, 81310 UTM Johor Bahru, Johor, Malaysia*

[c]*Department of Chemistry, Faculty of Science, Universiti Teknologi Malaysia, 81310 UTM Johor Bahru, Johor, Malaysia*

[d]*Malaysian Nuclear Agency, Kuala Lumpur, Malaysia*

† Electronic supplementary information (ESI) available. See DOI: 10.1039/c6ra06684d

been focused on improving the photocatalytic properties of the crystalline phases of TiO_2, as the amorphous TiO_2 (AT) structure has been reported to be a poorer photoactive substance due to its disordered structure and defective states.[12] Nevertheless, compared to crystalline TiO_2, AT has a larger surface area which leads to higher absorptivity and a high amount surface defects for enhancing the photoactivity.[13] Indeed, AT is easy to prepare, does not require any thermal treatment, has less demand for substrate materials and can be potentially deployed in practical applications. These useful characteristics have led to recent attention in exploring AT as an alternative to crystalline TiO_2 phases for various photocatalytic reactions.[12–15]

Previously, we reported a simple electrochemical method for preparing various metal oxides nanoparticles, such as Fe_2O_3, AgO, ZnO and NiO supported on zeolites and mesoporous silica. These catalysts were found to have a large potential in the photocatalytic reactions of organic pollutants and also carbon dioxide reforming of methane.[9,16–18] Accordingly, as an extension of this study, herein we report the preparation of CuO supported on AT. Characterization of the catalysts by XRD, N_2 adsorption–desorption, TEM, FTIR, XPS, ESR and UV-Vis DRS showed that the catalysts were rich with Ti^{3+} surface defects (TSD), oxygen vacancies (V_o), and Ti–O–Cu bonds. Ti–O–N bonds were also detected as a consequence of the ammonium salt used in the system. Significantly, photocatalytic testing of the oxidative desulfurization of dibenzothiophene (DBT) demonstrated that these species each played a role in enabling the photooxidation to be carried out under both UV and visible light irradiation. We believe that this new study which introduces metal ions onto AT could contribute to future design strategies for various catalysts in other reactions.

2.   Experimental

2.1   Materials

Ethanol, titanium(IV) isopropoxide (TTIP), dibenzothiophene (DBT), potassium peroxodisulfate, isopropanol, triethanolamine and sodium hydrogen carbonate were purchased from Merck Sdn. Bhd., Malaysia. Acetonitrile and iso-octane were obtained from QRec, Malaysia. Commercial TiO_2 (JRC-TiO_2-2) was provided by Catalysis Society of Japan. All of the chemicals were used as received without further treatment while tetraethylammonium perchlorate (TEAP) was synthesized by previous reported method.[19]

2.2   Synthesis of catalyst

The amorphous TiO_2 was prepared by sol–gel method. 4 mmol of TTIP was dropped into a mixture of ethanol (10 mL) and distilled water (0.9 mL) under constant stirring. During the addition of TTIP, a white precipitate was obtained and the suspension was further stirred for 30 min, aged for 24 h at room temperature and then, the beaker was placed in water bath at 313 K with constant stirring. At last, the white powder was obtained after dried in oven at 383 K for overnight and denoted as AT catalyst.

In this study, the copper oxide (CuO) nanoparticles were prepared according to previous reported method with some modification.[17,19–21] An open system electrolysis cell was fitted with a magnetic stirrer and a platinum plate cathode (2×2 cm^2) facing a copper plate anode (2×2 cm^2). A 10 mL distilled water was added into 0.1 M TEAP, which act as a supporting electrolyte. The electrolysis was conducted at a constant current of 120 mA cm^{-2} and 273 K under atmospheric pressure. After electrolysis, the obtained mixture was impregnated and dried at 383 K for 12 h to give black powder of the CuO nanoparticles. The CuO/TiO_2 catalysts with Cu contents varied from 5 to 20 wt% were prepared *via* the same procedure as CuO catalyst, except the AT powder was added to the mixture before the electrolysis started. The mixture was then impregnated and dried as above and ready for a characterization. The synthesized catalysts were denoted as 5, 10, 15 and 20 CAT. The required weight of the Cu supported on the TiO_2 was calculated based on duration time of the electrolysis according to the Faraday's law of electrolysis as follows:

$$t = \left(\frac{F}{I}\right)(z \times n) \tag{1}$$

where t is a total time for the constant current applied (s); F is Faraday constant, 96 486 C mol^{-1}; I is an electric current applied; z is a valency number of ions of substances (electrons transferred per ion); and n is an amount of substance (number of moles, liberated $n = m/M$).

For comparison, the crystalline CuO/TiO_2 catalysts were also prepared by impregnation (IMP) and physical mixing (PM) methods. For IMP method, 0.5 g of commercial TiO_2 was added into 10 mL distilled water, followed by 10 wt% CuO and then the mixture was impregnated at 313 K before oven dried overnight at 383 K. Similar procedure were carried out for the 15 wt% CuO and they denoted as 10 and 15 IMP, respectively. For PM method, same amount of commercial TiO_2 and CuO was mixed physically in the absence of distilled water and denoted as 10 and 15 PM.

2.3   Characterization of the catalyst

X-ray diffraction (XRD) analysis was carried out in a D8 ADVANCE Bruker X-ray diffractometer using Cu $K\alpha$ radiation at a 2θ angle ranging from $2°$ to $90°$. The phases were identified with the aid of the Joint Committee on Powder Diffraction Standards (JCPDS) files. The textural properties (*i.e.*, specific surface area and pore volume) were determined from N_2 adsorption–desorption at 77 K using a Beckman Coulter SA 3100 surface area analyzer. The samples were outgassed at 573 K for 1 h prior to the analysis. Surface areas were calculated from the N_2 adsorption isotherms using the Brunauer–Emmett–Teller (BET) method (S_{BET}). The morphological properties of the catalysts were examined by transmission electron microscopy (TEM, JEOL JEM-2100F). FTIR (PerkinElmer Spectrum GX FTIR Spectrometer) was performed using the KBr method with a scan range of 400–4000 cm^{-1}. The chemical oxidation state of the catalyst was determined using X-ray photoelectron spectroscopy (XPS) conducted on a Kratos Ultra spectrometer equipped with

an Mg Kα radiation source (10 mA, 15 kV) over a range of binding energies from 0 to 800 eV. The surface defect Ti^{3+} and oxygen vacancy were also confirmed using JEOL JESFA100 ESR spectrometer. The band gap energy of the catalysts were plotted based on the spectra recorded at room temperature over a range of wavelengths from 300 to 800 nm using a PIKE Technologies DiffusIR. The band gap is calculated according to the following formula,

$$E_g(eV) = \frac{1240}{\lambda} \qquad (2)$$

where E_g is the band gap (eV) and λ is the wavelength of the absorption edges (nm).

2.4 Photocatalytic oxidative desulfurization reaction

The photoactivities of the catalysts were evaluated by the oxidative desulfurization of dibenzothiophene (DBT). The experiments were performed in a batch reactor fixed with UV and visible lamps, and a cooling system. Model oil was prepared by dissolving DBT in iso-octane (100 mg L^{-1}) and in a typical reaction, 0.60–1.0 g L^{-1} catalyst was added to the reaction solution containing 50 mL model oil and acetonitrile. Then, the mixed solution was placed in the dark for 60 min with constant stirring to establish adsorption–desorption equilibrium. After that, the solution was irradiated with UV/visible lamp and the reaction solution were collected every 10 min and centrifuged before being analyzed by UV-Vis spectrophotometer (Thermo Scientific Genesys10uv Scanning). To ensure the accuracy, each set of experiments was performed three times. The above procedure was then repeated using the crystalline IMP and PM catalysts. The effect of different scavengers on photocatalytic performance was also evaluated using potassium peroxodisulfate (PP), isopropanol (IP), triethanolamine (TEOA) and sodium hydrogen carbonate (SHC). A certain amount of PP, IP, TEOA or SHC was added to the system before subjected to irradiation. Then, the sample was collected and analyzed using the same procedure as mention above.

3. Results and discussion

3.1 Structural studies

Fig. 1 illustrates the XRD diffractogram of the AT and CAT catalysts with different Cu loadings. As can be seen, no obvious characteristic peak for TiO_2 is found in the AT, except a broad peak between $2\theta = 20$–$30°$, indicating the presence of an amorphous structure. The inset figure shows the XRD pattern of the synthesized CuO with diffraction peaks located at $2\theta = 25.1$, 35.5, 36.4, 38.7, 48.7 and 61.5°.[22] For the CAT, similar characteristic peaks to AT were observed, proving the loading of Cu did not affect the amorphous phase of TiO_2. The peaks for CuO was clearly observed in 15 and 20 CAT (Fig. 1d and e), indicating the presence of CuO on the support.[23] The lack of CuO diffraction peaks on the 5 and 10 CAT may attribute to a diminutive amount of CuO to be detected by XRD.
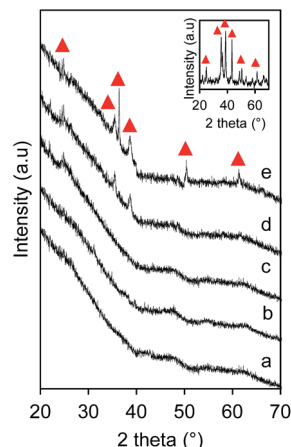

Fig. 1 XRD patterns of (a) AT, (b) 5 CAT, (c) 10 CAT, (d) 15 CAT, (e) 20 CAT and (inset figure) CuO.

3.2 Study of textural properties

N_2 adsorption–desorption isotherms were analyzed to investigate the surface area and pore size distribution of the catalysts. Fig. 2A shows that the catalysts exhibited a type IV isotherm with a H3 hysteresis loop, confirming a typical adsorption profile for a mesoporous material. From the figure, a remarkable two steps of capillary condensation were observed, with the first step at $P/P_o = 0.3$ and the second step at higher partial pressure, $P/P_o = 0.9$, which were assigned to intraparticle and interparticle mesopores, respectively.[24,25]

Based on the horizontal dotted reference line, the intraparticle pores of the AT were drastically reduced which consequently decreased the surface area and pore volume (Table 1) when Cu was added to prepare the CAT. Fig. 2B shows the Barrett–Joyner–Halenda (BJH) pore width distribution of the catalysts. It could be observed that the high intensity of the AT peak (inset figure) decreased gradually upon the addition of 5–15 wt% Cu, verifying the possibility of pore blockage due to the presence of the new metal particles on the surface of the AT.[24] In contrast, the pore volume and surface area increased when 20
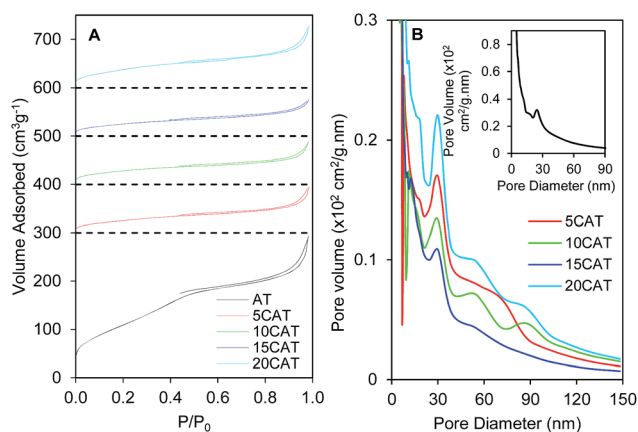

Fig. 2 (A) Nitrogen adsorption–desorption isotherm of catalysts, (B) pore distribution of catalysts, and (inset figure) AT.

Table 1 Textural properties of the catalysts

Catalyst	Surface area ($m^2 \ g^{-1}$)	Total pore volume ($\times 10^{-1} \ cm^3 \ g^{-1}$)	Band gap, E_g (eV)
AT	402	4.51	3.16
5 CAT	124	1.37	2.95
10 CAT	104	1.34	2.76
15 CAT	93	1.13	2.48
20 CAT	141	1.86	2.43
CuO	2	0.084	1.55
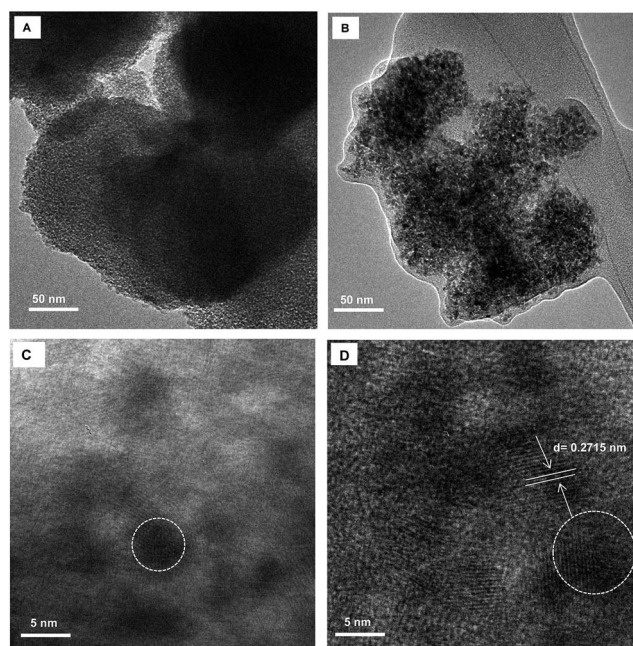
**Fig. 3** TEM images of (A) AT, (B and C) 10 CAT, and (D) HRTEM images of 10 CAT.

wt% of Cu was loaded onto the TiO_2, this may be due to the agglomeration of CuO on the TiO_2 surface leading to the formation of new pores.[26]

3.3 Morphological studies

The morphological properties of the AT and 10 CAT catalyst were examined by TEM and the images are presented in Fig. 3. Fig. 3A shows the well-defined mesoporous particles of the AT,[27] which supported the N_2 adsorption–desorption analysis. No obvious ordering, typical of a crystalline material, and no crystal grains formation on the image, consistent with the amorphous phase, were presented in the XRD results.[28] The black dots shown in Fig. 3B and C demonstrated the well dispersion of CuO nanoparticles on the AT surface, which was confirmed by its ∼0.2715 nm interplanar distance (*d*-spacing) for (1 1 0) lattice fringes (Fig. 3D).[29] The average particle sizes of CuO, in the range of 5–10 nm, shown in Fig. 3C proves the ability of this electrochemical method in synthesizing metal oxide nanoparticles.[9,16–18]

3.4 Vibrational spectroscopy

The catalysts were then subjected to FTIR analysis and the spectra in the region of 4000–400 cm^{-1} are shown in Fig. 4A. Generally, all catalysts show three main bands at 3452, 1650 and 535 cm^{-1}, which are attributed to O–H bending of molecularly physisorbed water, O–H bond of the hydroxyl group, and Ti–O–Ti bending vibration modes and/or CuO stretching, respectively.[4,30] All these bands decreased in intensity with increasing Cu, suggesting the possible perturbation of these groups by Cu species. In order to investigate the hydroxyl groups located on the AT, the catalysts were evacuated at 673 K for 1 h prior to FTIR measurement to remove the physisorbed water and the results are shown in Fig. 4B. Three main bands are observed at 3750, 3735 and 3715 cm^{-1}, which are ascribed to germinal and anatase phase hydroxyl groups, respectively.[31,32] The two former
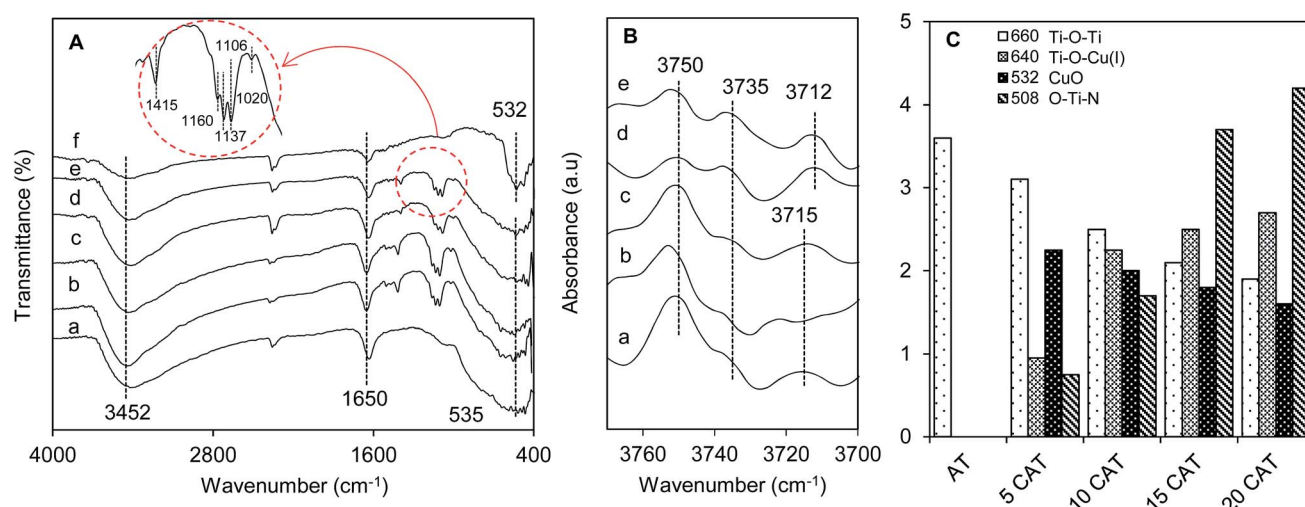
Fig. 4 (A) FTIR spectra of (a) AT, (b) 5 CAT, (c) 10 CAT, (d) 15 CAT, (e) 20 CAT and (f) CuO, (B) in evacuated system for region 3770–3700 cm^{-1}, (C) intensity of Gaussian peak area in the 800–400 cm^{-1} region.

bands considerably decreased with an increasing amount of Cu, confirming their interaction with the Cu species.[18,33] Similarly, the intensity of the latter band decreased and slightly shifted to 3712 cm^{-1}, particularly for a higher content of Cu loading, which usually referred to bridging hydroxyl group sites.[34] A weak band at 1415 cm^{-1} and triplet bands at 1160, 1137 and 1106 cm^{-1} were also observed for the CAT catalysts, which are assigned to the C–H and C–N stretching modes of the supporting electrolyte TEAP, respectively, while the band at 1020 cm^{-1} is supposedly due to the formation of the Ti–O–N bond.[35,36] These bands decreased with increasing Cu, signifying the possible consumption of the TEAP during the electrolysis.

For further investigation, a Gaussian curve-fitting for the band at 800–400 cm^{-1} was plotted (Fig. S1†), and the intensities of those bands are summarized in Fig. 4C. The AT consists of four strong bands at 735, 660, 564 and 475 cm^{-1}, which are assigned to Ti–O–Ti vibration modes.[37] Since all the Ti–O–Ti vibration bands showed a similar decreasing trend, the band at 660 cm^{-1} was chosen to represent the Ti–O–Ti vibration modes. For the CAT, three additional bands appeared at 640, 532 and 508 cm^{-1}, demonstrating the presence of Ti–O–Cu(ɪ), CuO and O–Ti–N bonds, respectively.[30,38,39] It was observed that the Ti–O–Ti and CuO vibrations decreased, while Ti–O–Cu(ɪ) and O–Ti–N increased with increasing Cu loading, and the changes of both Ti–O–Ti and O–Ti–N are somewhat obvious. All these FTIR results verified that the Ti–O–Ti was pertubated by the Cu species, as well as by N from the TEAP.

3.5 Chemical oxidation state determination

For detailed chemical property determination, the AT and 10 CAT were analyzed by XPS and the spectra are shown in Fig. 5. Fig. 5A presents the deconvolution results of XPS spectra of Ti 2p in the region of 470–455 eV. A clear single peak set (Ti 2p$_{1/2}$ and 2p$_{3/2}$), corresponding to the Ti^{4+} state, was observed for AT (Fig. 5A(a)), which markedly decreased in intensity and split to two peak sets of Ti^{4+} and Ti^{3+} states when Cu was introduced (Fig. 5A(b)).[40] It was clearly observed that approximately half of the Ti^{4+} ions were reduced to Ti^{3+} state in order to generate oxygen vacancies (V$_o$). The O 1s spectrum of AT (Fig. 5B(a))

consists of two peaks at 531.8 and 529.9 eV, which correspond to Ti–O–H and Ti–O–Ti, respectively.[41,42] Both also decreased in the same trend with the Ti 2p by the introduction of Cu accompanied by an emergence of two new peaks at 532.1 eV for Ti–O–N and 530.5 for Ti–O–Cu.[43,44] The sequence of these interactions toward oxygen could be explained by the electronegativity of each element, which is in the following order: N > H > Cu > Ti. Thus, fewer electrons at their neighbouring oxygen atom, leading to weaker electron–electron repulsion at the oxygen atom and hence increased binding energy of the electrons.[45]

The binding energy of the Cu 2p$_{3/2}$ peak (Fig. 5C) at around 935.1 eV and Cu 2p$_{1/2}$ peak (955.1 eV), together with the characteristic two shake-up features at binding energies of 941.5 and 944.1 eV, are an indicative of the Cu^{2+} species of CuO.[46] The other peaks observed at 933.1 and 952.6 eV correspond to Cu 2p$_{1/2}$, suggesting the presence of reduced copper species Cu$^+$, which further support the Ti–O–Cu(ɪ) species detected in the FTIR data.[47,48] The three peaks at 288.9, 287.9 and 284.5 eV shown in the C 1s spectra (Fig. 5D) are attributed to the C remained in the organic compound precursor or C–C, C–N and C–H bonds, respectively.[49,50] The peaks at 401.0 and 399.3 eV (Fig. 5E) are typically assignable to interstitial N atoms, normally referred to Ti–O–N and/or Ti–N–O,[51] respectively, which further support the presence of Ti–O–N bonds, as suggested by the FTIR. An immediate Ti–N bond is established between Ti and the introduced N atom, creating an N-induced mid-gap that narrows the band gap of the catalysts (Table 1).[52] The peak at 398.0 eV is similar to those of C 1s at 287.9 eV, which is attributed to the C–N bond, and the peak at 396.2 eV represents the existence of substitutional nitrogen in TiO$_2$ and these N atoms exist in the form of an O–Ti–N linkage.[52,53] From these XPS results, the formation of CuO, Ti–O–Cu(ɪ), O–Ti–N, Ti–O–N and/or Ti–N–O was confirmed and it supported all the observations from XRD, TEM and FTIR analyses.

The ESR spectroscopy is a very sensitive technique for studying the nature and crystal symmetry environment of catalysts. Thus, the synthesized catalysts were subjected to ESR and the spectra are presented in Fig. 6. Almost no peaks were
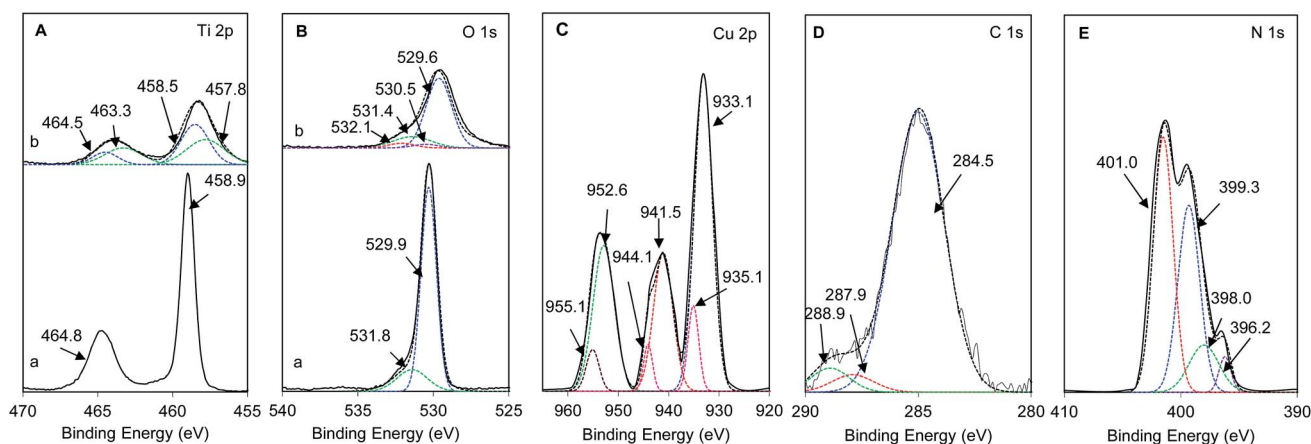

Fig. 5 (A) XPS spectra of Ti 2p (a) AT and (b) 10 CAT, (B) O 1s (a) AT and (b) 10 CAT, (C) Cu 2p, (D) C 1s and (E) N 1s of 10 CAT.
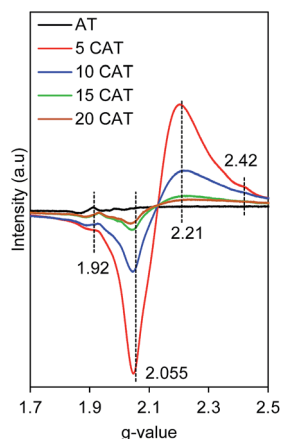
Fig. 6 ESR signals of the catalysts.

detected for AT, as Ti^{4+} has no unpaired electrons with paramagnetic nature. A strong signal was observed for the CAT at $g = 1.92$, corresponding to the Ti^{3+} surface defects (TSD), verifying the high concentration of V_o, supporting the XPS data.[54] This peak is also attributed to N$^{\cdot}$ radicals, while the $g = 2.055$, 2.42 and $g = 2.055$, 2.21 can be assigned to Cu^{2+} ions at the substitutional cation sites of TiO_2 and Cu^{2+} ions in CuO clusters, respectively.[55,56] It was observed that the CAT catalyst with lower Cu contents have a higher content of these paramagnetic centers.[57] Considering the FTIR results, in which the higher the Cu content, the lower the numbers of Ti–O–Ti and CuO, and the higher the formation of Ti–O–Cu(ı) and O–Ti–N bonds, as well as the consumption of TEAP, it could be dictated that the N and Cu atoms were incorporated in the oxygen vacancies in the TiO_2 matrix to enhance the structural stability.[58]

3.6 Proposed structure of the CAT catalyst

Based on the above characterization results, a plausible structure for the CAT catalysts is illustrated in Fig. 7. At the anode, the Cu plate was oxidized to Cu^{2+} ions, which are then reduced
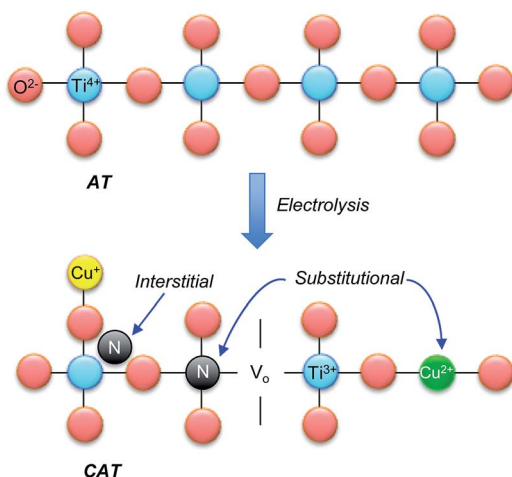

Fig. 7 Proposed structure for CAT catalyst.

at the cathode to form Cu^0 metal nanoparticles and subsequent drying gave the CuO clusters.[19–21] In parallel, the presence of the ammonium salt disrupted the AT matrix and led to ion exchange of Ti^{4+} with the N and Cu^{2+} ions to form Ti–O–N and Ti–O–Cu bonds.[36,45,59] V_o and TSD also formed, but the charge balancing by the further inclusion of N and Cu atoms stabilized the structure of the catalysts, mainly for higher Cu loading. In fact, the longer electrolysis time for higher Cu loading is most probably able to further reduce the Cu^{2+} ions to Cu^+ and triggered the higher TEAP consumption.[17,60] This might explain the formation of Ti–O–Cu(ı) bonds and bridging hydroxyl groups, as a consequence of the removal of Ti^{4+}.[31] The N atoms were also found to insert interstitially to form a N 1s state between the VB and the CB of the AT, accompanied with the inclusion of V_o, TSD and Cu, the band gap of CAT became narrower with increasing Cu loading.[61]

3.7 Photocatalytic oxidative desulfurization performance and proposed mechanism

Fig. 8A depicts the removal of dibenzothiophene (DBT) in a model oil over AT and CAT catalysts, after extraction and photooxidation for 90 min under UV light irradiation. Comparing to AT, the photocatalytic activity increased with increasing Cu loading from 5 to 10 wt%, demonstrating the enhancement in charge carrier separation by the incorporation of Cu and N in the CAT catalysts.[62] The Cu and N, as well as V_o and TSD, played roles as trapping sites to capture the photogenerated electrons from the CB and decreased the rate of electron–hole recombination, thus more electrons and holes are available for the reaction.[63] The photoactivity of the catalysts was in the following order: 10 CAT > 5 CAT > 15 CAT > AT. The 10 CAT showed the best extraction and photooxidation rate with 9.82×10^{-3} and 4.60×10^{-3} mM min^{-1}, respectively, but further increasing to 15 wt% Cu loading decreased the desulfurization activity. This may be due to the excess Cu loading on the surface of AT which blocked the UV light and inhibited the reaction rate.[17] Although the catalytic efficiency of the CAT catalysts slightly decreased when the desulfurization was carried out under visible light irradiation (Fig. 8B), they were active in both conditions. The performance of the best catalyst for both regions were also compared with the crystalline CuO/TiO_2 prepared by impregnation (IMP) and physical mixing (PM) methods, and the results are shown in Fig. S2.† It was observed that the 10 and 15 CAT showed higher desulfurization rate compared to those IMP and PM catalysts. This most probably due to the high surface area, narrow band gap and high amount of surface defects.[9] The high surface area allowed the adsorption of more DBT molecules and light harvesting for photooxidation to occur.[64] While, the narrow band gap and high amount of surface defects hindered the electron–hole recombination and enable photooxidation to be carried out in the visible light region. In order to further investigate the probable mechanism for DBT photooxidation over CAT catalysts, the effect of scavengers was studied for both UV- and visible-light systems and the results are shown in Fig. 8C and D. Four scavenging agents were used, potassium peroxodisulfate (PP), triethanolamine
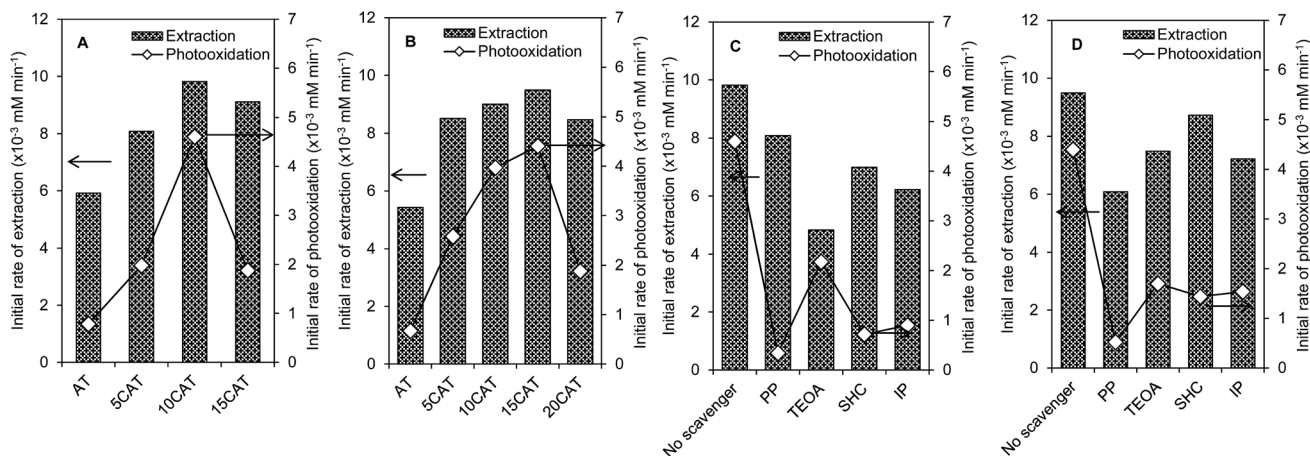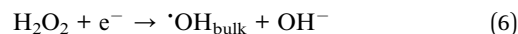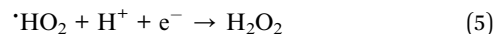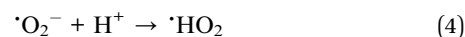
Fig. 8 Effect of different CuO loading on TiO$_2$ for sulfur removal (A) UV, (B) visible; sulfur removal efficiencies of DBT in the presence of electron scavenger, hole scavenger, $^{\bullet}OH_{ads}$ scavenger and $^{\bullet}OH_{bulk}$ scavenger by (C) 10 CAT catalyst [UV]; (D) 15 CAT catalyst [visible], [catalyst dosage is 0.8 g L^{-1}, initial concentration is 100 mg L^{-1}].

(TEOA), sodium hydrogen carbonate (SHC) and isopropanol (IP) with the roles of scavengers of photogenerated electrons (e$^-$), photogenerated holes (h$^+$), hydroxyl radicals adsorbed on the catalyst surface ($^{\bullet}OH_{ads}$) and hydroxyl radical ($^{\bullet}OH_{bulk}$), respectively.[24] Both systems showed that e$^-$ played the most important role in the photooxidation, followed by $^{\bullet}OH_{ads}$, $^{\bullet}OH_{bulk}$ and h$^+$. Comparing the photooxidation rate in the absence of a scavenger, the TEOA slightly inhibited the initial reaction rate. However, a greater inhibition of photocatalytic activity was observed using PP, confirming the significant role of the e$^-$, assisted by $^{\bullet}OH_{ads}$ and $^{\bullet}OH_{bulk}$. Accordingly, the photooxidation mechanism was proposed as illustrated in Fig. 9. Under UV irradiation (Fig. 9A), the electrons were excited from VB to CB of AT, and significantly the presence of CuO, defects structure (TSD and V$_o$) and impurity levels (N 1s and Cu 2p) hindered the e$^-$–h$^+$ recombination. The photogenerated e$^-$ then reduced the oxygen to superoxide anion radicals ($^{\bullet}O_2^-$), which is able to oxidize the DBT to DBTO$_2$.[64] As the desulfurization was conducted in open air system, even the iso-octane is

an organic solvent, the small amount of dissolved oxygen could also lead to the creation of $^{\bullet}OH_{bulk}$ via reaction of $^{\bullet}O_2^-$ with H$^+$ as follows,[65]

$$O_2 + e^- \rightarrow {}^{\bullet}O_2^- \tag{3}$$

$$^{\bullet}O_2^- + H^+ \rightarrow {}^{\bullet}HO_2 \tag{4}$$

$$^{\bullet}HO_2 + H^+ + e^- \rightarrow H_2O_2 \tag{5}$$

$$H_2O_2 + e^- \rightarrow {}^{\bullet}OH_{bulk} + OH^- \tag{6}$$

The H$^+$ ions might came from the surface's hydroxyl groups and hydroxyl groups of absorbed water vapor in the air.[64,66] In parallel with the formation of $^{\bullet}OH_{bulk}$, the generated h$^+$ in the VB also oxidized the H$_2$O or adsorbed OH$^-$ groups on the surface of AT to generate $^{\bullet}OH_{ads}$ to oxidize the DBT. Furthermore, the h$^+$ also directly oxidized the DBT to DBTO$_2$.[31] Other
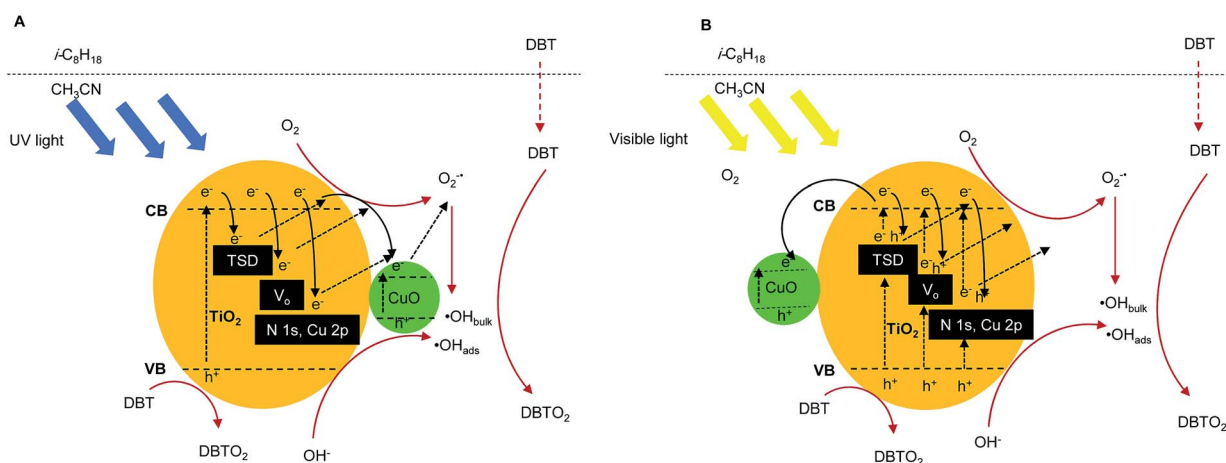

Fig. 9 Schematic illustration of DBT removal over CAT catalyst under (A) UV and (B) visible, [catalyst dosage 0.8 g L^{-1}, initial concentration is 100 mg L^{-1}].

than the role as electron capturers like CuO, the presence of TSD, V_o, N 1s and Cu 2p states between the VB and CB of CAT lowered its band gap and enabled photooxidation to be carried out in the visible light region (Fig. 9B). The electron excitation from the VB to TSD, V_o, N 1s and Cu 2p states and from that levels to CB led to the generation of electron–hole pairs.[64] Subsequent reactions of the e^- and h^+ toward photooxidation of DBT are same as under the UV irradiation.

3.8 Kinetic studies

To study the kinetics of DBT photooxidation, a series of reactions at different initial concentrations of DBT, ranging from 100 to 300 mg L^{-1}, were performed. Generally, the influence of the initial concentration of the solution on the photocatalytic degradation rate of most organic compounds is described by pseudo first-order kinetics, which is rationalized in terms of the Langmuir–Hinshelwood model, modified to accommodate reactions occurring at the solid–liquid interface.[17] At low initial DBT concentrations, the simplest equation for the rates of photooxidation of DBT is given by,
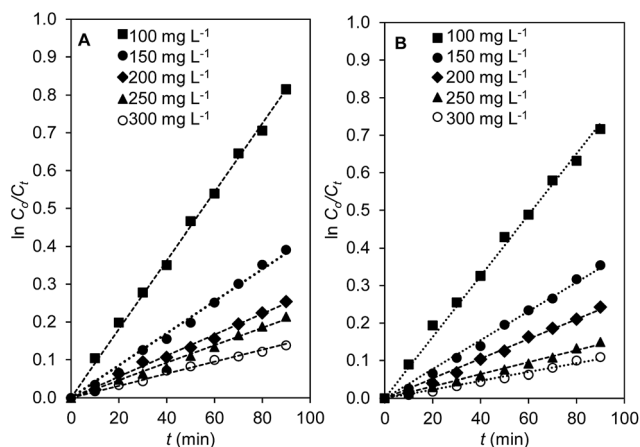
$$\ln C_t = -kt + \ln C_o \tag{7}$$

Fig. 10 (A) Photooxidation kinetics of DBT using 10 CAT catalyst at different initial concentrations under UV, (B) photooxidation kinetics of DBT using 15 CAT catalyst at different initial concentrations under visible, [catalyst dosage is 0.8 g L^{-1}].

where k is the pseudo first-order rate and C_o and C_t are the concentrations of DBT initially and at time t, respectively.[67] The integration of eqn (7) yields (8),

$$\ln\left(\frac{C_o}{C_t}\right) = kt \tag{8}$$

The linearity of the plot of $\ln(C_o/C_t)$ vs. irradiation time verified that the reaction process approximately followed the pseudo-first order kinetics model (Fig. 10). The slope of the line is the apparent first-order rate constant (k_{app}). The values of k_{app} obtained from our experiments are listed in Table 2 and reveal a significant and favorable effect of the CAT catalysts on the photooxidation of DBT. The value of k_{app} decreased with increasing initial concentration, demonstrating the system was favorable at low concentrations.[9]

An increase in initial concentration inhibited light penetration to the surface of the catalyst and thus reduced the formation of the superoxide and hydroxyl radicals which play such an important role in the photooxidation. The line with an intercept of $1/k_r$ and $1/k_r K_{LH}$ was obtained from the Langmuir–Hinshelwood (L–H) kinetic formula (eqn (9)):

$$\frac{1}{k_{app}} = \left[\frac{1}{k_r K_{LH}}\right] + \frac{C_o}{k_r} \tag{9}$$

where k_r is the reaction rate constant (mg L^{-1} min^{-1}), K_{LH} is the adsorption coefficient of the reactant (L mg^{-1}) and C_o is the initial concentration of DBT (mg L^{-1}). The calculated values of k_r and K_{LH} were 0.381 mg L^{-1} min^{-1} and 0.045 L mg^{-1} for UV and 0.353 mg L^{-1} min^{-1} and 0.032 L mg^{-1} for visible. Because the value of k_r is larger than K_{LH}, these results suggested that the DBT adsorption on the surface of the CAT was the controlling step of the process. A similar phenomenon was reported previously for the photodecolorization of methyl orange over α-Fe_2O_3-supported HY as a photocatalyst.[16]

3.9 Other applications

The potential of 10 and 15 CAT catalysts were also examined on a photodegradation of other organic compounds; methylene blue (MB) and 2-chlorophenol (2-CP) and the results are demonstrated in Fig. 11. Under UV light region, 10 CAT able to degrade 73.2% of MB and 85.9% of 2-CP with the rate of 1.97×10^{-4} and 6.22×10^{-4} mM min^{-1}, respectively. While, fairly higher degradation were achieved by 15 CAT under visible light

Table 2 Photooxidation of DBT at different initial concentration and pseudo-first-order apparent constant values [catalyst dosage 0.8 g L^{-1}]

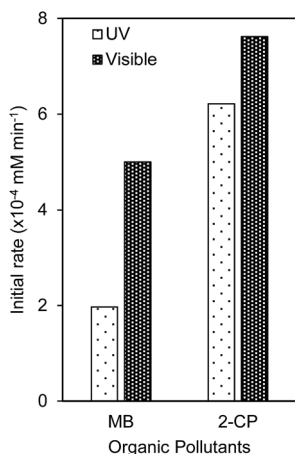| Initial conc. C_o (mg L^{-1})	UV		Visible	
	Rate, k_{app} ($\times 10^{-3}$ min^{-1})	Initial rate, r_o ($\times 10^{-1}$ mg L^{-1} min^{-1})	Rate, k_{app} ($\times 10^{-3}$ min^{-1})	Initial rate, r_o ($\times 10^{-1}$ mg L^{-1} min^{-1})
100	9.1	5.68	8.1	5.35
150	4.2	4.99	3.9	4.29
200	2.8	4.59	2.6	4.40
250	2.5	4.79	1.6	2.90
300	1.6	3.59	1.2	2.39

Fig. 11 Photodegradation of organic pollutants using 10 CAT and 15 CAT.

region, where 84.9% for MB and 93.4% for 2-CP with the rate of 5.0×10^{-4} mM min^{-1} and 7.62×10^{-4} mM min^{-1}, respectively. These results evidenced the high potential of catalysts to be applied in various applications.

4. Conclusions

In summary, a simple sol–gel method was used to prepare amorphous TiO_2 nanoparticles and incorporation with 5–20 wt% Cu by an electrochemical method was used to produce CAT catalysts. The physicochemical properties of the synthesized catalysts were studied by XRD, N_2 adsorption–desorption, TEM, FTIR, XPS, ESR and UV-Vis DRS. The FTIR and XPS analyses verified the presence of CuO, Ti–O–Cu, Ti–O–N and O–Ti–N bonds, while the presence of TSD and V_o was verified by ESR analysis. The photocatalytic testing of oxidative desulfurization of dibenzothiophene (DBT) under UV and visible light irradiation exhibited the effectiveness of the CAT in both conditions. A study of the effects of scavengers showed that the photogenerated electron was the key factor in the photooxidation, followed by hydroxyl radicals adsorbed on the catalyst surface ($^{\bullet}OH_{ads}$), hydroxyl radical ($^{\bullet}OH_{bulk}$) and holes. The TSD, V_o, N 1s and Cu 2p states played an important role as electron capturers to hinder the electron–hole recombination and enhance the photooxidation. These species narrowed the band gap of CAT which enabled photooxidation to be carried out in the visible light region. The photooxidation followed a pseudo-first order Langmuir–Hinshelwood model with adsorption being the controlling step. It is believed that further investigation in this area would contribute to a better understanding on the potential use of metal oxides/amorphous TiO_2 catalysts for the abatement of various organic pollutants.

Acknowledgements

References

1 K. S. Triantafyllidis and E. A. Deliyanni, *Chem. Eng. J.*, 2014, **236**, 406.

2 V. C. Srivastava, *RSC Adv.*, 2012, **2**, 759.

3 M. Zhang, W. Zhu, S. Xun, H. Li, Q. Gu, Z. Zhao and Q. Wang, *Chem. Eng. J.*, 2013, **220**, 328.

4 C. Wang, W. Zhu, Y. Xu, H. Xu, M. Zhang, Y. Chao, S. Yin, H. Li and J. Wang, *Ceram. Int.*, 2014, **40**, 11627.

5 G. Dedual, M. J. MacDonald, A. Alshareef, Z. Wu, D. C. W. Tsang and A. C. K. Yip, *J. Environ. Chem. Eng.*, 2014, **2**, 1947.

6 A. A. Jalil, M. A. H. Satar, S. Triwahyono, H. D. Setiabudi, N. H. N. Kamarudin, N. F. Jaafar, N. Sapawe and R. Ahamad, *J. Electroanal. Chem.*, 2013, **701**, 50.

7 W. Zhu, Y. Xu, H. Li, B. Dai, H. Xu, C. Wang, Y. Chao and H. Liu, *Korean J. Chem. Eng.*, 2013, 7.

8 L. Wang, Y. Chen, L. Du, S. Li, H. Cai and W. Liu, *Fuel*, 2013, **105**, 357.

9 N. F. Jaafar, A. A. Jalil, S. Triwahyono, J. Efendi, R. R. Mukti, R. Jusoh, N. W. C. Jusoh, A. H. Karim, N. F. M. Salleh and V. Suendo, *Appl. Surf. Sci.*, 2015, **338**, 84.

10 M. Liu, H. Li and W. Wang, *Catal. Today*, 2015, **264**, 242.

11 S. Buddee, S. Wongnawa, U. Sirimahachai and W. Puetpaiboool, *Mater. Chem. Phys.*, 2011, **126**, 177.

12 J. Huang, Y. Liu, L. Lu and L. Li, *Res. Chem. Intermed.*, 2012, **38**, 487.

13 K. Kaur and C. V. Singh, *Energy Procedia*, 2012, **29**, 291.

14 Y. Li, T. Sasaki, Y. Shimizu and N. Koshizaki, *J. Am. Chem. Soc.*, 2008, **130**, 14755.

15 H. H. Pham and L. Wang, *Phys. Chem. Chem. Phys.*, 2015, **17**, 541.

16 N. F. Jaafar, A. A. Jalil, S. Triwahyono, M. N. M. Muhid, N. Sapawe, M. A. H. Satar and H. Asaari, *Chem. Eng. J.*, 2012, **191**, 122.

17 N. W. C. Jusoh, A. A. Jalil, S. Triwahyono, H. D. Setiabudi, N. Sapawe, M. A. H. Satar, A. H. Karim, N. H. N. Kamarudin, R. Jusoh, N. F. Jaafar, N. Salamun and J. Efendi, *Appl. Catal., A*, 2013, **468**, 276.

18 S. M. Sidik, A. A. Jalil, S. Triwahyono, T. A. T. Abdullah and A. Ripin, *RSC Adv.*, 2015, **5**, 37405.

19 A. A. Jalil, N. Kurono and M. Tokuda, *Tetrahedron*, 2002, **58**, 7477.

20 A. A. Jalil, N. Kurono and M. Tokuda, *Synlett*, 2001, 1944.

21 A. A. Jalil, N. Kurono and M. Tokuda, *Synthesis*, 2002, 2681.

22 N. F. Khusnun, A. A. Jalil, S. Triwahyono, N. W. C. Jusoh, A. Johari and K. Kidam, *Phys. Chem. Chem. Phys.*, 2016, **18**, 12323.

23 Z. L. Liu, Z. L. Cui and Z. K. Zhang, *Mater. Charact.*, 2005, **54**, 123.

24 N. W. C. Jusoh, A. A. Jalil, S. Triwahyono, A. H. Karim, N. F. Salleh, N. H. R. Annuar, N. F. Jaafar, M. L. Firmansyah, R. R. Mukti and M. W. Ali, *Appl. Surf. Sci.*, 2015, **330**, 10.

25 K. Zhao, Y. Lu, N. Lu, Y. Zhao, X. Yuan and H. Zhang, *Appl. Surf. Sci.*, 2013, 1.

26 S. M. Sidik, S. Triwahyono, A. A. Jalil, M. A. A. Aziz, N. A. A. Fatah and L. P. Teh, *J. CO₂ Util.*, 2016, **13**, 71.

27 M. C. Kimling, D. Chen and R. A. Caruso, *J. Mater. Chem. A*, 2015, **3**, 3768.

28 G. Bertoni, E. Beyers, J. Verbeeck, M. Mertens, P. Cool, E. F. Vansant and G. V. Tendeloo, *Ultramicroscopy*, 2006, **106**, 630.

29 H. F. M. Zaid, F. K. Chong and M. I. A. Mutalib, *Fuel*, 2015, **156**, 54.

30 K. Rajaram, E. Savarimuthu and S. Arumugam, *Chem. Sci. Rev. Lett.*, 2014, **8**, 626.

31 R. Jusoh, A. A. Jalil, S. Triwahyono and N. H. N. Kamarudin, *RSC Adv.*, 2015, **5**, 9727.

32 H. Lin, J. Long, Q. Gu, W. Zhang, R. Ruan, Z. Li and X. Wang, *Phys. Chem. Chem. Phys.*, 2012, **14**, 9468.

33 M. A. A. Aziz, A. A. Jalil, S. Triwahyono and M. W. A. Saad, *Chem. Eng. J.*, 2015, **260**, 757.

34 O. B. Belskaya, V. K. Duplyakin and V. A. Likholobov, *Smart Nanocompos.*, 2011, **1**, 1949.

35 S. Jesurani, S. Kanagesan, R. Velmurugan, C. Thirupathi, M. Sivakumar and T. Kalaivani, *Mater. Lett.*, 2011, **65**, 3305.

36 Z. Zhang, Z. Huang, X. Cheng, Q. Wang, Y. Chen, P. Dong and X. Zhang, *Appl. Surf. Sci.*, 2015, **355**, 45.

37 R. Urlaub, U. Posset and R. Thull, *J. Non-Cryst. Solids*, 2000, **265**, 276.

38 W. Lin and H. Frei, *C. R. Chim.*, 2006, **9**, 207.

39 N. T. Nolan, D. W. Synnott, M. K. Seery, S. J. Hinder, A. V. Wassenhoven and S. C. Pillai, *J. Hazard. Mater.*, 2012, **211–212**, 88.

40 B. Chen, V. Nguyen, J. C. S. Wu, R. Martin and K. Kočí, *Phys. Chem. Chem. Phys.*, 2016, **18**, 4942.

41 R. Bashiri, N. M. Mohamed, C. F. Kait and S. Sufian, *Int. J. Hydrogen Energy*, 2015, **40**, 6021.

42 D. Barreca, G. Carraro, A. Gasparotto, C. Maccato, O. I. Lebedev, A. Parfenova, S. Turner, E. Tondello and G. V. Tendeloo, *Langmuir*, 2011, **27**, 6409.

43 Y. Cong, J. Zhang, F. Chen and M. Anpo, *J. Phys. Chem. C*, 2007, **111**, 6976.

44 B. Guo, Q. Zhang, G. Li, J. Yao and C. Hu, *Green Chem.*, 2012, **14**, 1880.

45 N. W. C. Jusoh, A. A. Jalil, S. Triwahyono and C. R. Mamat, *Appl. Catal., A*, 2015, **492**, 169.

46 L. Chiang and R. Doong, *J. Hazard. Mater.*, 2014, **277**, 84.

47 J. Yu, Y. Hai and M. Jaroniec, *J. Colloid Interface Sci.*, 2011, **357**, 223.

48 Z. Liu and C. Zhou, *Prog. Nat. Sci.*, 2015, **25**, 334.

49 J. Yang, H. Bai, X. Tan and J. Lian, *Appl. Surf. Sci.*, 2006, **253**, 1988.

50 Z. He, W. Que, J. Chen, Y. He and G. Wang, *J. Phys. Chem. Solids*, 2013, **74**, 924.

51 Y. Zhang, K. Cheng, F. Lv, H. Huang, B. Fei, Y. He, Z. Ye and B. Shen, *Colloids Surf., A*, 2014, **452**, 103.

52 Z. Zhang, Z. Huang, X. Cheng, Q. Wang, Y. Chen, P. Dong and X. Zhang, *Appl. Surf. Sci.*, 2015, **355**, 45.

53 J. Yang, H. Bai, X. Tan and J. Lian, *Appl. Surf. Sci.*, 2006, **253**, 1988.

54 H. Song, T. G. Jeong, Y. H. Moon, H. H. Chun, K. Y. Chung, H. S. Kim, B. W. Cho and Y. T. Kim, *Sci. Rep.*, 2014, **4**, 4350.

55 I. Ardelean, M. Peteanu, R. Ciceo-Lucacel and I. Bratu, *J. Mater. Sci.: Mater. Electron.*, 2000, **11**, 11.

56 G. Li, N. M. Dimitrijevic, L. Chen, T. Rajh and K. A. Gray, *J. Phys. Chem. C*, 2008, **112**, 19040.

57 N. Kruse, A. Frennet and J. M. Bastin, *Stud. Surf. Sci. Catal.*, 1997, 116.

58 E. A. Konstantinova, A. I. Kokorin, K. Lips, S. Sakhtivel and H. Kisch, *Appl. Magn. Reson.*, 2009, **35**, 421.

59 N. F. M. Salleh, A. A. Jalil, S. Triwahyono, J. Efendi, R. R. Mukti and B. H. Hameed, *Appl. Surf. Sci.*, 2015, **349**, 485.

60 I. D. dos Santos, J. C. Afonso and A. J. B. Dutra, *J. Braz. Chem. Soc.*, 2011, **22**(5), 875.

61 L. G. Devi and R. Kavitha, *RSC Adv.*, 2014, **4**, 28265.

62 M. M. Joshi, N. K. Labhsetwar, P. A. Mangrulkar, S. N. Tijare, S. P. Kamble and S. S. Rayalu, *Appl. Catal., A*, 2009, **357**, 26.

63 Y. Ma, X. Wang, Y. Jia, X. Chen, H. Han and C. Li, *Chem. Rev.*, 2014, **114**, 9987.

64 M. Zarrabi, M. H. Entezari and E. K. Goharshadi, *RSC Adv.*, 2015, **5**, 34652.

65 A. Groysman, *Corrosion in Systems for Storage and Transportation of Petroleum Products and Biofuels*, 2014.

66 L. Xiong, J. Li, B. Yang and Y. Yu, *J. Nanomater.*, 2012, 13.

67 F. Lin, Y. Zhang, L. Wang, Y. Zhang, D. Wang, M. Yang, J. Yang, B. Zhang, Z. Jiang and C. Li, *Appl. Catal., B*, 2012, **127**, 363.